

RESEARCH ACTIVITIES OF STRUCTURAL MECHANICS AND DYNAMICS GROUP, SAITAMA UNIVERSITY IN 2008-2011

Hiroki YAMAGUCHI¹⁾, Yoshiaki OKUI¹⁾ and Yasunao MATSUMOTO²⁾
¹⁾ Professor, ²⁾ Associate Professor
Department of Civil and Environmental Engineering, Saitama University

ABSTRACT

This report gives the recent research activities of the Structural Mechanics & Dynamics Group, Saitama University, during the period from 2008 to 2011. The research projects conducted in the group include 1) flexural strength of steel-concrete girders, 2) experimental study on flexure-shear coupling strength of composite girders, 3) effect of base isolation bearing's modeling on seismic response, 4) vibration-based structural health monitoring, 5) interpretation of field-measured of field-measured wind-induced vibrations in transmission lines, 6) noise generation from modular bridge expansion joint, and 7) human response to vibration. The outline and findings of some of these research projects are summarized in this report.

KEYWORDS: composite girder, load-carrying capacity, design code, web slenderness limit, base-isolation bearing, modal damping, gust response, seismic response, structural health monitoring, modal identification, cable system, wind-induced vibration, gust response, transmission line, expansion joint noise, vibro-acoustic analysis, environmental vibration, vibration perception, human body dynamics, vibration discomfort.

1. INTRODUCTION

The Structural Mechanics and Dynamics Group has a responsibility of research and education on structural engineering problems in the Department of Civil and Environmental Engineering, Saitama University. The group consists of three faculty members whose names are listed above as authors of this report.

The objective of this report is to briefly describe the recent research activities of the group from 2008 to 2011.

2. FLEXURAL STRENGTH OF STEEL-CONCRETE GIRDERS

A bridge high performance steel with a yield strength of 500MPa has been standardized as SBHS500 in JIS since 2008. SBHS500 shows advantages as high yield strength, good weldability, but it has different inelastic behavior, such as almost no yield plateau, smaller ductility, and greater yield ratio, if comparing to conventional grade steels. Application of SBHS500 to hybrid girders is expected to be an economical solution for composite girder bridges. However, no studies have ever tried to investigate the bending moment capacity of SBHS500 hybrid girders. In this chapter, the web

slenderness limits for section classification of homogeneous and hybrid girders using SBHS500 with consideration of the initial bending moment will be presented.

2.1 Nonlinear FE Analyses

A parametric study with the nonlinear FE analysis is carried out to investigate the web slenderness limits for composite girders with SBHS500 steel. In the parametric study, the web depth b_w and the concrete slab thickness t_c are kept constant as 3000 and 300 mm, respectively. On the other hand, the web thickness is assigned to obtain width-thickness ratios of 200, 158, 120; and the dimensions of the flange plates and concrete slab width are changed to obtain various positions of the neutral axis. In total, 87 and 98 girder models were analyzed for homogeneous and hybrid sections, respectively.

In FE analyses, a half of the steel-concrete composite I-girders are meshed based on symmetry of the model structure and loading condition. The flanges and web are modeled by 4-node thin shell elements; concrete slab is modeled with 8-node solid elements. To simulate the unshored construction method, the phase analysis is employed. The effect of initial bending moment can be considered in the phase analysis. The magnitudes of the initial bending moment are assigned to $M_I = 0.2; 0.4; 0.6$

M_{ys} , where M_{ys} is the yield bending of steel girder section only.

The elasto-plastic steel material behavior is modeled by the Prandtl-Reuss equation and von Mises yield criterion. The uniaxial multi-linear stress-strain curves of steel grade SM490Y for the web plate and SBHS500 for the flange plates are shown in Figure 1, which are based on experimental results. Concrete in compression is modeled as linear-elastic, plastic hardening material and Mohr-Coulomb yield criterion. The uniaxial stress-strain curve for concrete under compression is shown in Figure 2 (JSCE, 2007). The initial geometric imperfection in the web plate is considered as a sinusoidal form. The maximum initial out-of-plane displacement is assigned to $b_w/250$ according to Japanese ‘‘Specifications for Highway Bridges’’ (Japan Road Association, 2002):

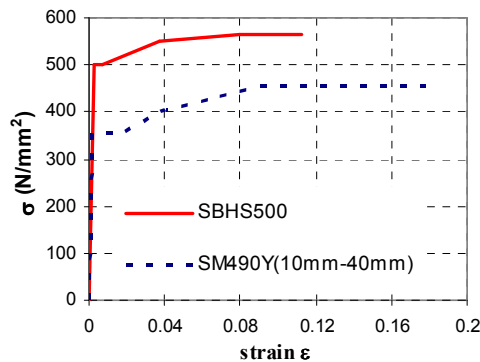


Figure 1 Uniaxial stress-strain relation applied for steel material models

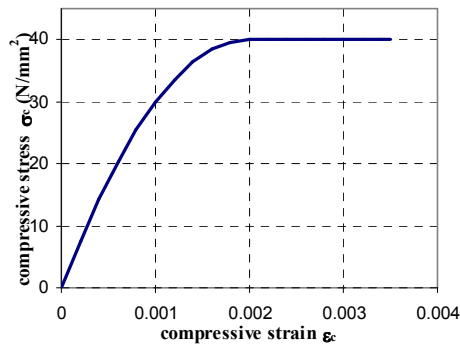


Figure 2 Compression uniaxial stress-strain curves applied for concrete material model

2.2 SBHS500 homogeneous section

In this section, FE analysis results of SBHS500 homogeneous girders along with the web slenderness limit of AASHTO, Eurocode and the previous results (Gupta et al., 2006) will be presented. Figure 3 shows the web slenderness boundary between compact and noncompact sections, in which b_w/t_w and α present the width-thickness ratio and the parameter of the compres-

sion region of web plate, respectively. In this figure, the black symbols stands for the numerical results judged as compact sections, while the green ones for noncompact sections. The SBHS500 homogeneous sections for the initial bending moment $M_1=0$ present significant greater web slenderness limit than those of AASHTO, Eurocode and proposed by Gupta et al. The inelastic behavior of SBHS500 steel seems to be the main reason. Owing to the smaller yield plateau of SBHS500, it can sustain a greater plastic local buckling strength than conventional steel.

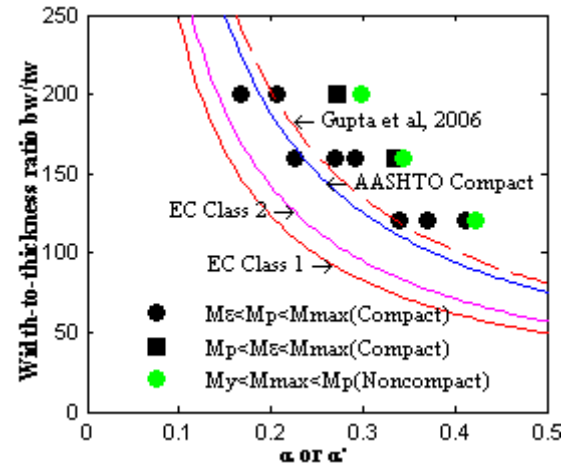


Figure 3 Compact-noncompact limit of homogeneous SBHS500 steel section ($M_1=0$)

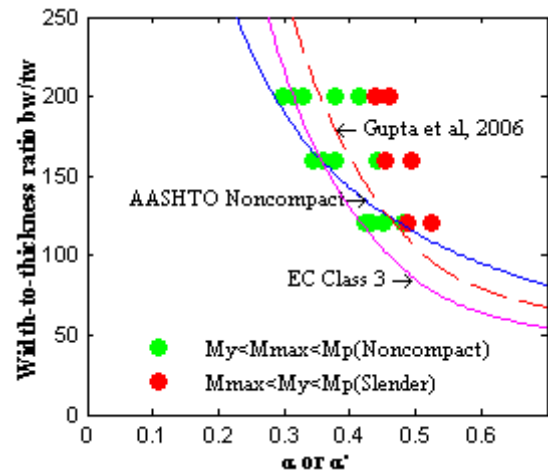


Figure 4 Noncompact-slender limit of homogeneous SBHS500 steel sections ($M_1=0$)

3. EXPERIMENTAL STUDY ON FLEXURE-SHEAR COUPLING STRENGTH OF COMPOSITE GIRDERS

The interaction between the bending moment and shear capacities of composite girders is investigated experimentally. The experimental study was

implemented with 3 test girders, which have the same cross section shown in Figure 5, but different span lengths to obtain different combinations of bending moment and shear force. The test setup was designed with 3-point loading as shown in Figure 6. The I-shaped steel girders were designed with SM400A grade steel, whose design yield strength $f_y = 300$ MPa, and the design material strength of concrete slab is 45 MPa.

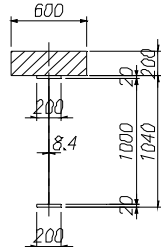


Figure 5 Cross section of test girders

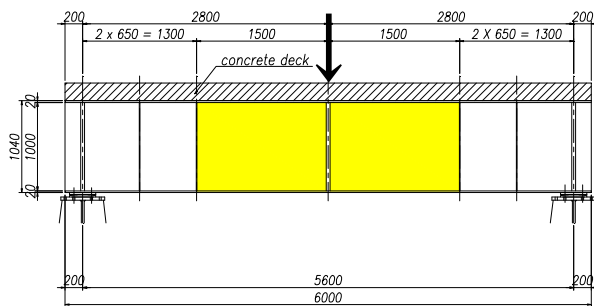


Figure 6 Side view of test girder (Case-1))

The applied load in each loading step and the corresponding deflection at the span center were measured and plotted in Figure 7. The out-of-plane displacements at limit points on the test web panel were also recorded.

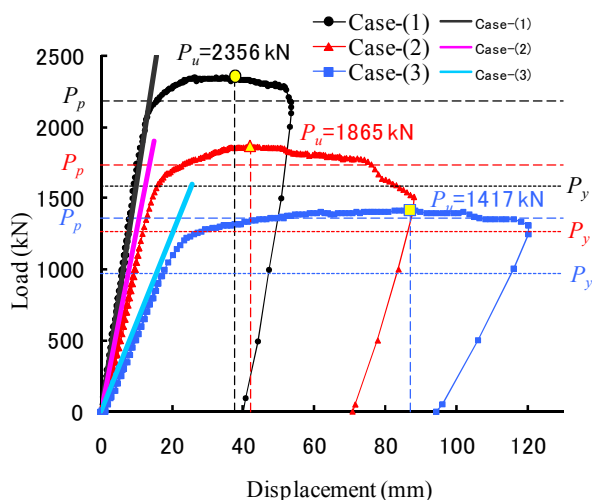


Figure 7 Load-deflection curves of three specimens

Table 1 lists the bending moment and shear force obtained from the experiments at the ultimate state as well as the full plastic bending moment and the ultimate shear force based on Basler equation. Figure 8 presents the moment-shear strength interaction equations in an old version of AASHTO and Eurocode as well as experimental results including the present three experiments. It is seen from the collected experimental data that there is no reduction of the bending moment capacity due to the moment-shear interaction effect.

Table 1 Ultimate flexural and shear strength

	Ultimate strength (Measurement value)		Ultimate strength (Calculate value)	
	M_u (kNm)	Q_u (kN)	M_p (kNm)	$Q_{(Basler)}$ (kN)
Case-(1)	3298	1178	3061	1149
Case-(2)	3264	933	3033	1149
Case-(3)	3259	709	3127	1171

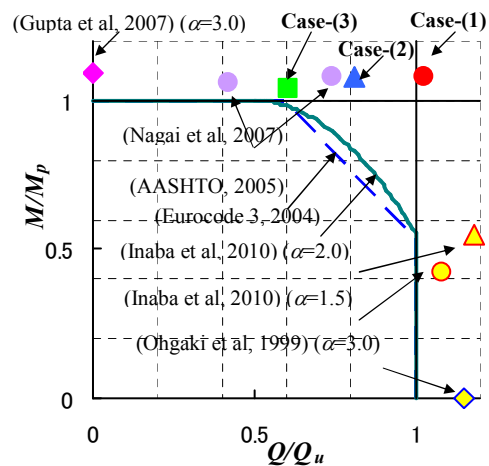


Figure 8 Interaction between bending moment capacity and shear capacity

4. EFFECT OF BASE ISOLATION BEARING'S MODELING ON SEISMIC RESPONSE

The effects of modeling of isolation bearings on the seismic response of bridges are investigated. To this end, a nonlinear dynamic analysis of a viaduct with natural rubber bearings (RBs), lead rubber bearings (LRBs) and high damping rubber bearings (HDRBs) is carried out. Three analytical models of isolation bearings are considered for comparison: the equivalent linear model, the conventional bilinear model, and the rate-dependent rheology model developed by the authors.

4.1 Model bridge

Figure 9 shows the physical model of a five-span continuous steel-concrete composite girder bridge isolated by laminated rubber bearings. As the laminated rubber bearings, three types of isolation bearings are considered: high damping rubber bearings (HDRBs), lead rubber bearings (LRBs) and natural rubber bearings (RBs). The isolation bearings are installed between the steel girders and the tops of the piers. The dimensions of this model bridge including rubber bearings are determined by designing in accordance with Japanese Specifications of Highway Bridges (JRA 2002). The dimensions and material properties of the isolation bearings are presented in Table 2.

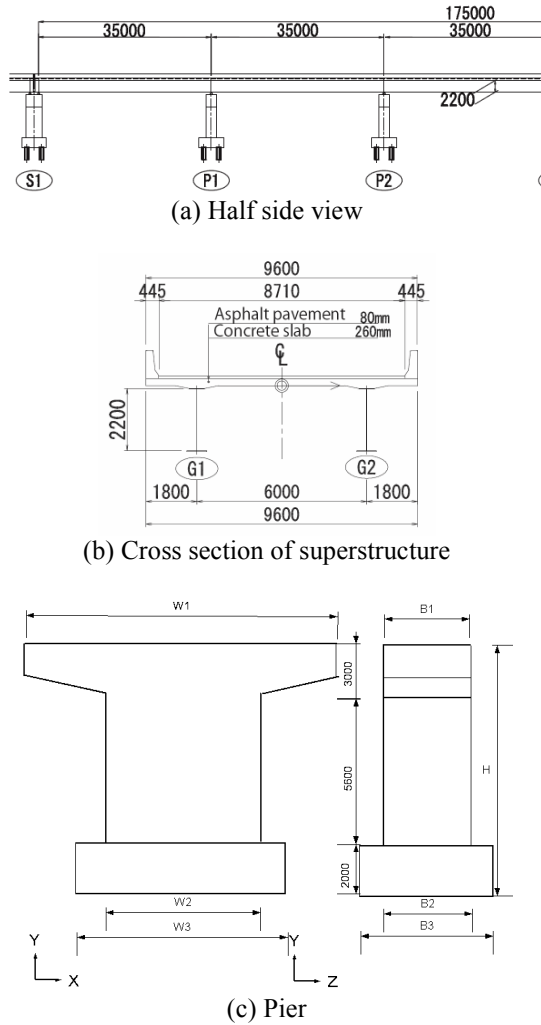


Figure 9 Description of the bridge (All dimensions are in mm)

Table 2 Properties of the isolation bearings

Dimension	Specifications		
	RB	LRB	HDRB
Length (mm)	650.0	650.0	650.0
Width (mm)	650.0	650.0	650.0
Total thickness of rubber layers (mm)	81.0	81.0	81.0
Material type	G12	G12	G12

The entire structural system is approximated as 2-D frame. The superstructure is idealized as an elastic beam. The plastic behavior of piers is expected to concentrate at the bottom of piers, where plastic hinges are occurred. The plastic behavior of the hinges is modeled by the tri-linear Takeda model (Takeda et al. 1970). The superstructure, the pier cap, the pier body except the plastic zone, and the footing are modeled using the simple elastic beam elements. The foundation and soil-structure interaction are idealized by a set of linear translational and rotational springs.

4.2 Modeling of rubber bearings

In order to describe the mechanical behavior of isolation bearing, two types of analytical models of the bearings are used in the study: the rate dependent rheology model as developed by the authors (Bhuiyan et al. 2009a; 2009b) and the design models including the bilinear model and the equivalent linear model specified in JRA (2002).

The rheology model (Bhuiyan et al. 2009) is illustrated in Figure 10, where τ and γ are the average shear stress and shear strain of rubber layers, respectively. In this model, the total shear stress is decomposed into three contributions associated with a nonlinear elastic stress, an elasto-plastic stress and finally a viscosity induced overstress as given in

$$\tau = \tau_{ep}(\gamma_a) + \tau_{ee}(\gamma) + \tau_{oe}(\gamma_c) \quad (1)$$

where

$$\tau_{ep} = C_1 \gamma_a \begin{cases} \gamma_s \neq 0 & \text{for } |\tau_{ep}| = \tau_{cr} \\ \gamma_s = 0 & \text{for } |\tau_{ep}| < \tau_{cr} \end{cases}$$

$$\tau_{ee} = C_2 \gamma + C_3 |\gamma|^m \text{sgn}(\gamma)$$

$$\tau_{oe} = A \frac{|\dot{\gamma}|^n}{|\dot{\gamma}|} \text{sgn}(\dot{\gamma}) \quad \tau_{oe} = C_4 \gamma_c$$

$$A = \frac{1}{2} (A_1 \exp(q|\gamma|) + A_u) + \frac{1}{2} (A_1 \exp(q|\gamma|) - A_u) \tanh(\xi \tau_{oe} \gamma_d)$$

$$\dot{\gamma}_d = 1/\text{sec}$$

and C_i ($i = 1$ to 4), τ_{cr} , m , A_1 , A_u , q , n , and ξ are parameters of the model to be determined from experimental data (Bhuiyan 2009).

4.3 Seismic response of bridge

Due to symmetry of the bridge structure shown in Figure 9 and due to space limitation, only one pier's results P1 (=P4) using HDR bearing are graphically presented and discussed herein. Figure 10 shows the moment-rotation relations of the plastic hinges of the pier for level-2 type-II earthquake. The similar trend of the responses is obtained from the shear stress-strain relations of the bearings as shown in Figure 11. The effect of modeling of isolation bearings on the responses of the bridge have been clearly appeared in the comparisons of maximum shear strain (γ_{max})

occurred in the isolation bearings and the ratio of the maximum rotation to the allowable rotation of the plastic hinge.

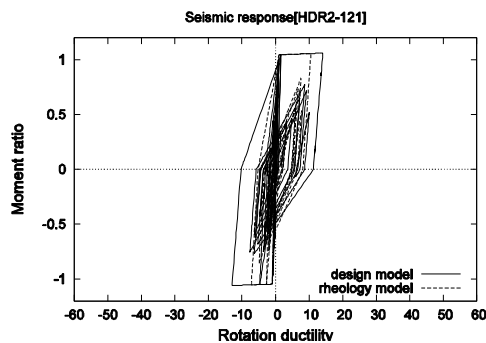


Figure 10 Moment-rotation relationships at plastic hinge of the pier P1 (=P4) as obtained for HDR2 bearings due to level-2, type-II earthquake; moment ratio (M/M_y) is the bending moment (M) at the level of plastic hinge divided by the yield moment (M_y) and rotation ductility is the rotation occurred at the plastic hinge level divided by the yield rotation.

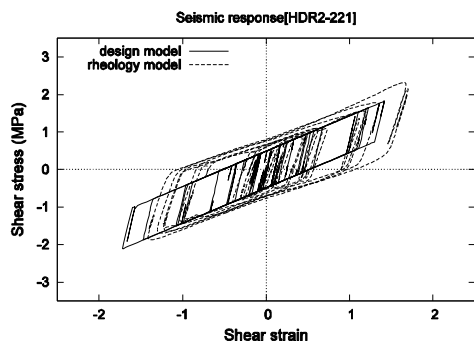


Figure 11 Shear stress-strain relationships of the isolation bearing (HDR2) located at the top of the P1 (=P4) piers due to level-2, type-II earthquake.

5. VIBRATION-BASED STRUCTURAL HEALTH MONITORING

Structural health monitoring has been one of the most important issues in structural engineering recently, and there have been a number of research activities in this field all over the world. Some of the studies conducted in the Structural Mechanics and Dynamics have been published in Yoshioka et al. (2010a) in Japanese, part of which has been described in English in Matsumoto et al. (2010) and Yoshioka et al. (2010b, 2011). The objective of this study was to study the feasibility of vibration-based structural health monitoring in steel truss bridges. Sets of vibration measurement were conducted at an existing steel truss bridge with local

damages found recently (Figure 12). The results presented in the following sections show a possibility of the identification of local damages in steel truss bridges, such as damages in diagonal members, from changes in the modal properties of the structure obtained from vibration measurements.



Figure 12 Steel truss bridge investigated

5.1 Natural frequency changes in local vibration modes

Impact testing of the diagonal members was conducted in those with damage and without so as to identify the effect of damage on local vibration characteristics of the tension diagonal members. A three-axis accelerometer unit consisting of three single-axis piezoelectric accelerometers was attached to the flange of tension diagonal members at the quarter point from the bottom. Impacts were applied by an impact hammer to the web of the diagonal member at the quarter point from the bottom.

Figure 13 shows an example of the results of impact testing that compares the Fourier spectra of the response to impact of a diagonal member D1 with pitting corrosions (referred to as corroded in the figure) and that of a D1 without corrosion (referred to as healthy). In the figure, the stabilization diagram obtained from the Eigensystem Realization Algorithm, ERA (Juang and Pappa 1985) for the diagonal member without corrosion is compared with the corresponding Fourier spectrum. The Modal Amplitude Coherence, MAC, was used to identify reliable natural frequencies in the ERA. The comparison between the Fourier spectrum and the stabilization diagram from the ERA implies that the natural frequency identified from the measurement records in the impact testing were reliable.

It was observed that the natural frequencies observed at frequencies above 100 Hz were different between healthy and corroded diagonal members, while there were minor differences in the frequency range below 100 Hz (Figure 13). The natural frequencies of the diagonal member with pitting corrosions appeared to be lower than those of the diagonal member without corrosions. Similar

trend were found with the comparison between this diagonal member with pitting corrosions and other healthy diagonal members with nominally the same dimensions. The decreases in the natural frequencies in the frequency range above 100 Hz for the corroded diagonal member may be associated with decreases in the modal stiffness of higher order local vibration modes that are attributed to the pitting corrosions.

The natural frequencies of higher order local vibration modes of diagonal members can be a direct indicator of damages, although a practical implementation of the identification of natural frequencies of a number of diagonal members may need further development. A possible solution may be applying impact testing only on diagonal members that are identified as critical members in redundancy analysis.

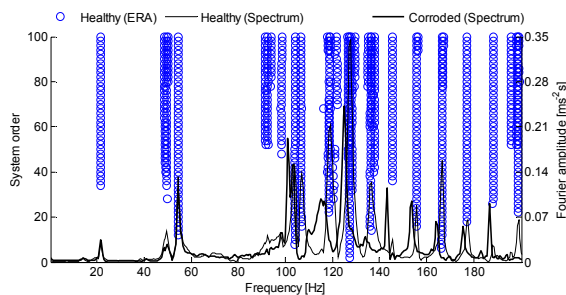


Figure 13 Fourier spectra of response of healthy and corroded diagonal members to impact. Stabilization diagram from ERA obtained for health diagonal member are also shown.

5.2 Damping change in coupled vibration mode

In order to identify the effect of damages on the dynamic characteristics of the bridge vibration of the bridge was measured at three locations: the lower chord members on both sides of the bridge and a longest tension diagonal member, D5. The number of measurement locations was limited because the measurement needed to be made during a short time period between the detection of the damages and the urgent reinforcement of the diagonal members. The measurement was conducted in the span with the local fracture found and, for comparison, in a span without damages. The acceleration of the lower chord member was measured in the vertical direction at the quarter point of the span. The accelerations in three orthogonal axes were measured in D5 at the quarter point from the bottom. Vibration of the bridge was induced by a dump truck with a total mass of about 200 kN running at different speeds between 20 and 40 km/h while the bridge was closed to other traffic.

It was understood that there were closely spaced vibration modes at frequencies around the

natural frequencies of the diagonal members. This was partly because there were four diagonal members in a span that had nominally the same dimensions. In addition to vibration modes dominated by the motion of the diagonal members (referred to as a local mode in this paper), there were coupled vibration modes between the diagonal members and the whole structure (referred to as a coupled mode).

Figure 14 shows the changes in the modal frequencies and damping ratios before and after the reinforcement of the diagonal members identified in the measurement. The modal properties shown in the figure were obtained by the ERA. The figure shows that, in the local vibration mode dominated by the motion of the diagonal member damaged and repaired, the modal frequency increased from 7.1 Hz to 9.8 Hz, approximately, and the modal damping ratio decreased from 0.0055 to 0.0039 after the reinforcement. In the global vibration modes involving the motion of the whole structure, there appeared to be changes in the modal damping ratio with minor changes in the modal frequency. It was noted that there was more variability in the identification of the modal damping ratio from the measurement records in the lowest order vibration modes, such as the mode at about 2.6 Hz in the figure, although the data are not presented in this paper. This variation in the damping was considered to be caused by the friction damping at the bearing supports that was dependent heavily on the displacement amplitude of vibration. In the global mode at about 7.3 Hz, however, there was less variability in the identification of modal damping ratio and the change in the modal damping shown in Figure 14 was more reliable than the changes in the lowest order vibration modes.

The identification of changes in the damping of global mode may be more practical in terms of the feasibility of measurement, compared to impact testing of all diagonal members, although there is a need to improve the reliability of the identification of modal damping.

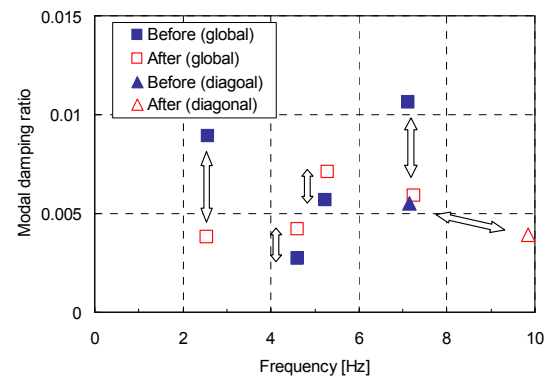


Figure 14 Examples of changes in modal frequencies and damping ratios before and after reinforcement of diagonal members.

6. INTERPRETATION OF FIELD-MEASURED WIND-INDUCED VIBRATIONS IN TRANSMISSION LINES

After Den Hartog's explanation of large wind-induced vibrations in iced conductors as galloping, any form of large vibrations in transmission line system have been thought to be caused by the galloping type instability. However, the issue is embroiled by recent accidents due to large vibrations of the system in gusty winds. Both in-plane and out-of-plane vibrations can be important in causing accidents like loosening of bolts, breaking of insulators attachments and breaking of porcelain plates. In order to control such large vibrations, it is indispensable to clearly identify type of these vibrations as gust response or galloping. The objective of this study was to interpret field-measured vibrations based on measured data analysis and gust response analysis.

Tokyo Electric Power Company (TEPCO) has been recording wind-induced vibrations of its overhead transmission lines with multiple bundled conductors both in iced and un-iced conditions. In this study, the vibration data with the wind data recorded by TEPCO has been analyzed for two different types of transmission lines, which were selected because some damages were reported in different components of these transmission lines due to large wind-induced vibrations. The maximum peak-to-peak amplitudes (MPPAs) observed were, for example, about 7m in the out-of-plane direction, 5m in the in-plane vertical direction and 70 degree in the torsional direction. Such large span-vibrations can result in the dynamic response of components such as insulator and spacer leading to their damage. The objectives of the field measurements were, therefore, set to clearly identify the causes of vibrations that could have caused the damages in different components of transmission lines.

Figure 15 shows the geometries of the studied transmission lines with the instrumentation for the field measurement. The M-I Line has single span; 615m long, between two anchoring towers. On the other hand, the S-B Line has two spans; 635m and 407m long, anchored at the intermediate tower and connected through a jumper line that might change the dynamic characteristics of the transmission line system. It should be noted that the numbers of bundled conductors are eight and four for the M-I Line and the S-B Line, respectively. TEPCO has measured the accelerations in all three translational directions and the torsional velocity by the accelerometers and the angular velocimeter, respectively, at the quarter and mid spans as shown in Figure 1. For the measurement of wind velocity, the three dimensional ultrasonic anemometer was placed at the top of tower. The measurement data used in this study are all the measured vibration events and the

vibration events with wind data from December 2008 to July 2009.

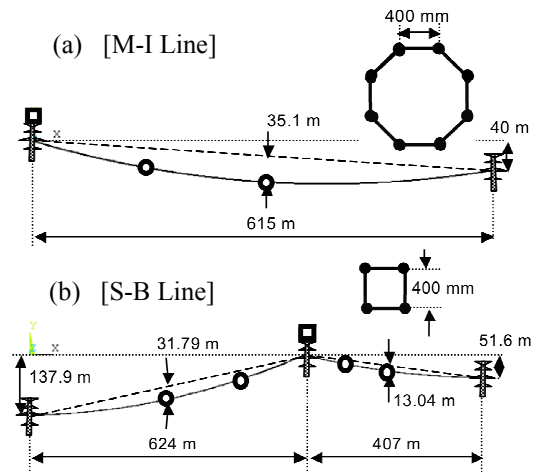


Figure 15 Geometries of the transmission lines and cross-section of bundled conductors: (a) M-I Line, (b) S-B Line.

A Finite Element (FE) program, ANSYS, was used to carry out the eigenvalue analysis based on the FE models of the transmission lines. Cubic polynomial based cable elements were used for electric conductors with zero bending stiffness. Spacers were modeled as rigid beam elements and insulators, consisting of small links were modeled with cable elements with zero bending stiffness. It should be noted that the rotation of each conductor could be freed or fixed depending upon the tightness of spacer clamp affecting the torsional stiffness of bundled conductors. Therefore the transmission line was modeled with different types of spacers and it was found that the form of spacer did not change torsional frequencies significantly as long as the connection between spacer and conductor was rigid.

The characteristics of field measured vibrations in frequency domain can be understood by the analytically evaluated natural frequencies and mode shapes. Figure 16 shows an interesting phenomenon in the S-B Line, that is a coupling of span and jumper vibrations. Such coupling is important as it can induce very large vibration in jumper and result into its damage. To interpret the coupled response in the S-B Line, the power spectral densities of field measured jumper and 407 m span L/2 vibrations are plotted in the figure. Three dominant peaks of the jumper torsional, span torsional and jumper lateral responses appear at almost the same frequency of about 0.36 Hz. Appearance of the peaks at the same frequency can be due to the linear coupling in the span and jumper vibration modes as indicated in Figure 16 as one of the FE analysis results.

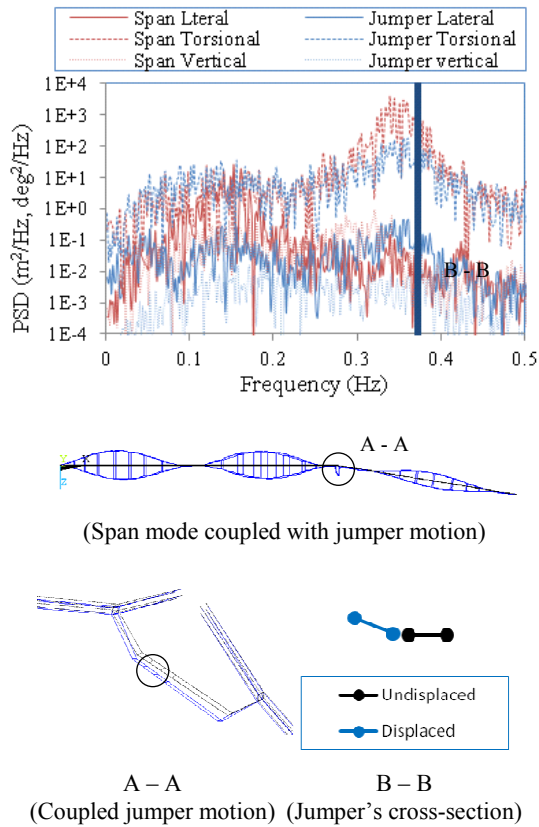


Figure 16 Power spectral density (PSD) of span-jumper responses in S-B Line and corresponding coupled mode with natural frequency of 0.373 Hz.

Gust response analysis was carried out in the frequency domain by using the measured wind data. The power spectral density (PSD) of response based on Davenport's theory can be derived by using usual frequency domain formulation, neglecting the aerodynamic interaction among conductors. The response PSD was first calculated for each event and the response RMS was next evaluated by numerically integrating the spectrum. In the analysis, the following assumptions were introduced for the parameters. The drag coefficient for un-iced single conductor normally ranges from 1.25 to 0.89 and an average value of 1.07 was assumed in the analysis. The aerodynamic admittance for transmission lines can be taken as one. The value of k was taken as 15 by considering its general range from 10 to 20. As for the modal damping ratios, constant values of 5% and 3% are assumed for the out-of-plane and in-plane responses, respectively, while the damping in transmission line might be dominated by aerodynamic damping which may be increased with the increase of mean wind velocity.

Despite of small discrepancies in higher frequency ranges in the case of in-plane response of M-I Line, the agreement between measured and calculated PSDs was very good especially in domi-

nant frequency ranges. Figure 17 compares the gust response analysis results with the field measured responses for the S-B Line. The RMS response is compared for all measured vibrations data available for particular point in the transmission lines. Discrepancies in RMS response are due to imperfection in estimation of aerodynamic damping that can vary from event to event and due to small peak in wind spectra that can exaggerate if located near or at the same frequency of resonant peaks.

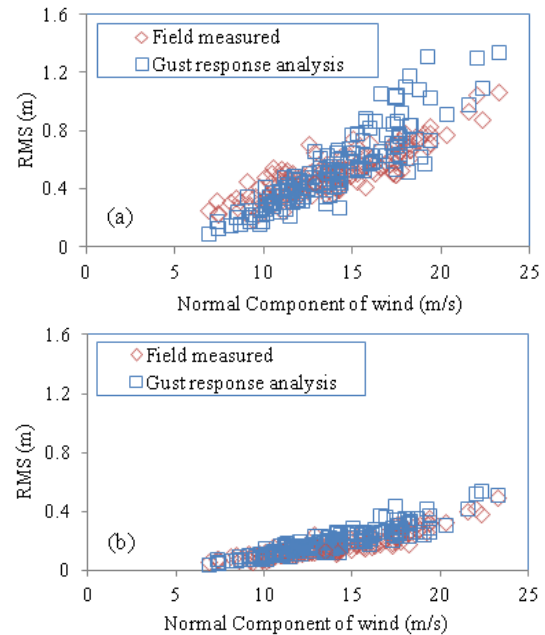


Figure 17 RMS responses in S-B Line, 407m span $L/2$: (a) Out-of-plane responses, (b) In-plane responses.

Detailed full-scale measurements of the responses of the M-I Line and the S-B Line, and associated wind conditions, have enabled interpretation of field observed vibrations based on the gust response analysis. High turbulence intensities and parabolic pattern of RMS responses verses mean wind velocity indicate the possibility of observed vibrations as gust responses. Reasonable agreement between the calculated and the observed response spectra and RMS responses further confirms that observed vibrations could be gust responses, in which the lower modes contribute more to the response compared with higher modes. However, there might be a possibility of galloping phenomena in the transmission line systems and more vivid interpretation is required in future.

7. NOISE GENERATION FROM MODULAR BRIDGE EXPANSION JOINT

The modular-type expansion joint, which divides the total movement capacity into several small gaps by the use of steel middle-beams, has

been developed and applied in highway bridges. However, noise generated from modular bridge expansion joints during vehicle pass-bys has caused localized environmental problems in Japan and elsewhere. The research group has therefore been studying the characteristics and control of the noise for the modular expansion joints, focusing on a possible mechanism of noise generation. The previous research report of the group (Yamaguchi et al. 2008) has described experimental investigations (e.g., Ravshanovich et al. 2007, Matsumoto et al. 2007). In this report, numerical investigations of the mechanism of sound generation and radiation (Ghimire et al. 2008, 2009) are introduced.

7.1 Vibro-acoustic analysis of noise generation from a full scale model of modular expansion joint

Previous experimental studies (e.g., Ravshanovich et al. 2007, Matsumoto et al. 2007) showed that possible causes of dominant noise components generated from the bottom side of the modular bridge expansion joint might be different from those from the top side. The objective of this study was to obtain theoretical insights into the mechanism of noise generation from the bottom side of the joint for which a main noise source might be structural vibration of the joint.

Vibro-acoustic analysis was conducted based on the information from a full-scale model of modular expansion joint obtained in previous experimental studies. Figure 18 shows the full-scale joint model investigated. The joint model was set up in the compound of the Kawaguchi Metal Industries Co., Ltd. in Saitama, Japan. The joint model was mounted on top of a test cavity constructed under the ground level to represent the cavity beneath the joint between adjacent bridge girders in real bridges (Figure 19). There was an opening at each end of the cavity. The wall of the cavity was covered by the Styrofoam that provided sound absorption within the cavity.

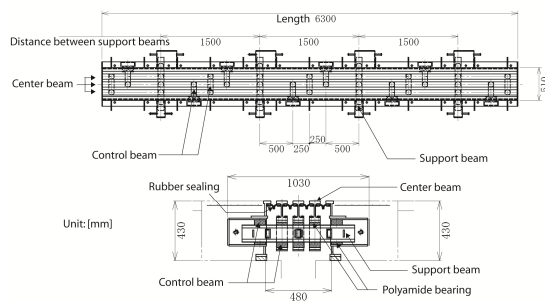


Figure 18 Plan and cross-sectional views of the full-scale joint model.

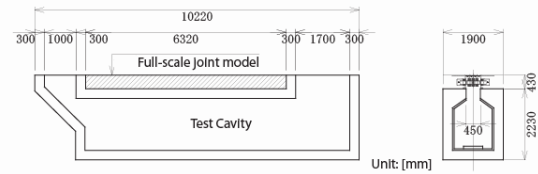


Figure 19 Cross-sectional views of the cavity beneath the joint

The dynamic behavior of the joint model was investigated by using the finite element method (FEM) and the sound field inside the cavity located beneath the joint model was analyzed by using the boundary element method (BEM). Indirect BEM was used to calculate the sound pressure inside the cavity with the velocity response obtained by the FE analysis as a boundary condition. The frequency range considered in the analysis was 20-400 Hz where dominant frequency components were observed in the noise measured in the cavity beneath the joint in the previous experiment. It was intended to interpret numerical results obtained by a model developed with available mechanical properties of the joint components to seek a general understanding of the noise generation mechanism of the modular expansion joint.

Figure 20 compares the sound pressure inside the cavity calculated from the models and that measured in the previous experiments. The natural frequencies of structural vibration modes of the joint and the acoustic resonance frequencies of the cavity are also shown in the figure. It was observed that the peaks in the spectrum of noise inside the cavity were due to resonances of structural vibration modes of the joint and/or resonances of acoustic modes of the cavity (Figure 20). There was evidence that showed possible interaction between structural modes of the joint and the acoustic modes of the cavity.

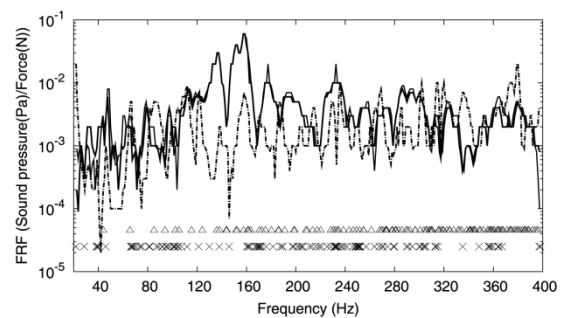


Figure 20 Sound pressure inside the cavity and natural frequencies of structural and acoustic modes. Key: - . - . . , model; ———, experiment-1; ———, experiment-2; X, structural mode; Δ, acoustic mode

The peaks in the frequency response function calculated for the sound pressure in the cavity, as observed in Figure 20, may be attributed to three different mechanisms: (1) major contribution of structural mode(s) of the joint with possible minor contribution of acoustic mode(s) of the cavity, (2) significant contribution from both structural mode(s) of the joint and acoustic mode(s) of the cavity, and (3) major contribution of acoustic mode(s) of the cavity with possible minor contribution of structural mode(s). For example, the peak in the frequency response function for the sound pressure at around 160 Hz in Figure 20 may be attributed to the resonance of the structural mode at 160.35 Hz and the acoustic modes at 161.10 Hz and 161.71 Hz. These structural and acoustic modes are shown in Figure 21. The acoustic mode at 161.10 Hz shown in Figure 21 had low amplitude at the boundary with the joint so that this acoustic mode may have had little interaction with the structural mode. Although the acoustic mode at 161.71 Hz shown in Figure 21 may have had higher possibility of interaction with the structural mode, the magnitude around the measurement point of this acoustic mode was low. Therefore, the peak in the frequency response function for the sound pressure at around 160 Hz may be caused mainly by the excitation of the structural mode with some minor effects from the acoustic modes. Similar discussion could be made on each peak of the frequency response function for the sound pressure so that the mechanism of noise generation are either (1), (2) or (3) described above..

7.2 Numerical investigation of noise generation and radiation from a modular expansion joint in an existing bridge

The objective of this study was to understand the mechanisms of noise generation and radiation from an existing modular bridge expansion joint installed in an expressway bridge to the surrounding area (Figure 22). First, field measurements of the noise and vibration of the expansion joint under its operating conditions were conducted. A numerical investigation, the main content of this study, was then conducted to understand the mechanisms of noise generation and radiation. In the numerical investigation, the modular expansion joint, the cavity and the surrounding sound field were considered to be a vibro-acoustic system. Frequency responses of this system were calculated using the finite element method–boundary element method (FEM–BEM) approach with harmonic dynamic loadings applied to the joint as an input and sound pressures in the sound field around the joint as an output so as to understand the fundamental dynamic and acoustic characteristics of the vibro-acoustic system. The dynamic analysis of the joint was carried out by FEM and the sound fields inside the cavity located beneath the joint and outside of

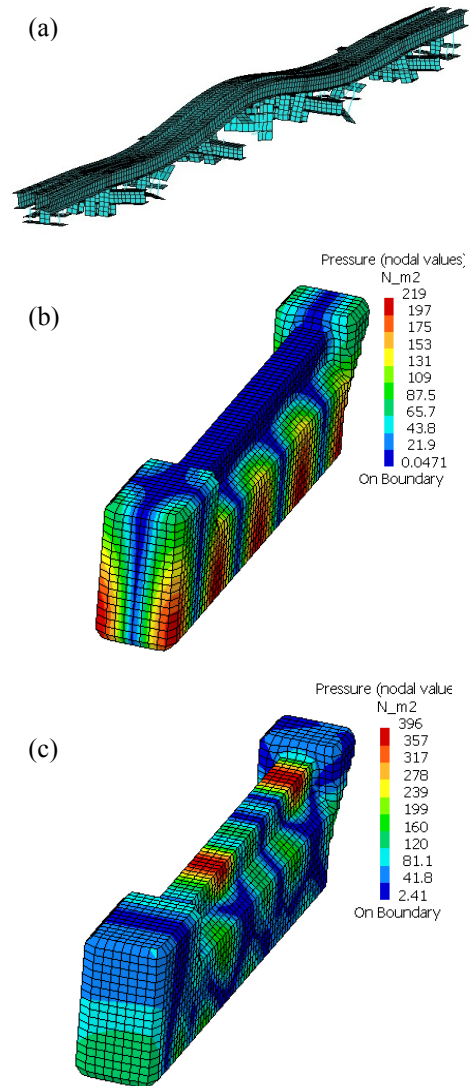


Figure 21 Structural and acoustic modes generating sound around 160 Hz: (a) Structural mode at 160.35 Hz; (b) Acoustic mode at 161.10 Hz and (c) Acoustic mode at 161.70 Hz.



Figure 22 The prestressed bridges with modular type expansion joints investigated

the cavity were analyzed by BEM. The structural modal properties of the joint and the acoustic modal properties of the cavity were obtained in FE analyses of the joint and cavity, respectively, and used to interpret the frequency responses calculated for the vibro-acoustic system.

Figure 23 shows the sound pressure at a point inside the cavity, calculated numerically with a harmonic load applied to a location where loadings might be applied during a vehicle pass-by. Figure 23 also shows the sound pressure recorded at the corresponding point in the measurement during a heavy truck pass-by. Although the magnitudes of the sound pressure response obtained from the numerical analysis cannot be compared directly with those obtained in the measurements, some similarities were observed in the numerical analysis and the measurement, such as dominant frequency components. In addition, the natural frequencies of the structural modes of the joint and the natural frequencies of the acoustic modes of the cavity obtained numerically are compared with the sound pressures in the figure.

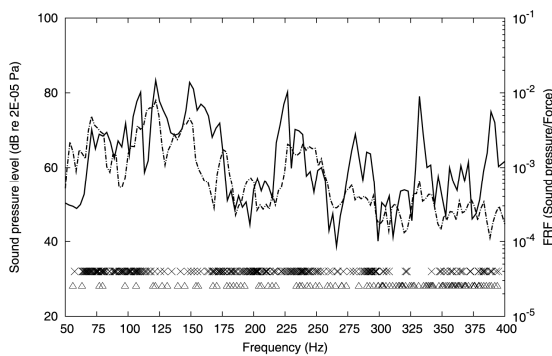


Figure 23 Sound pressure response inside the cavity. — analysis; - - - experiment; X natural frequency of structural mode; Δ natural frequency of acoustic mode.

It is important to understand the sound radiation characteristics of the joint–cavity system with respect to the environmental problem. The cavity beneath the joint was surrounded by the PC girders of the bridge and the concrete pier, as shown in Figure 22. The sound generated inside the cavity may propagate outside mainly from the two open ends of the cavity along its longitudinal axis. The directivity of sound radiation was calculated so as to identify the radiation characteristics of the sound in the vertical plane passing through the middle of the cavity along its length. Several concentric directivity circles having their center at the center of joint–cavity system were considered. Their radii varied from 8 m to 100 m at intervals of 4 m. The sound pressure was calculated at points on each circle's circumference at an angular interval of 3°.

The angles were measured in anti-clockwise direction from the horizontal axis which was parallel to the longitudinal axis of the cavity. The effect of ground was not included in the analysis.

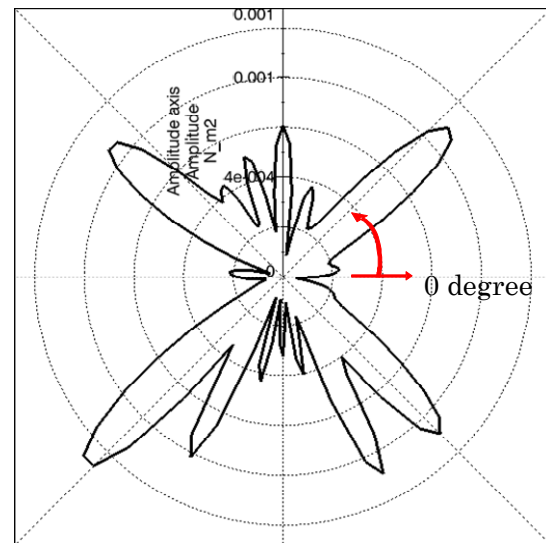


Figure 24 Sound radiation pattern at 149 Hz at a distance of 12 m

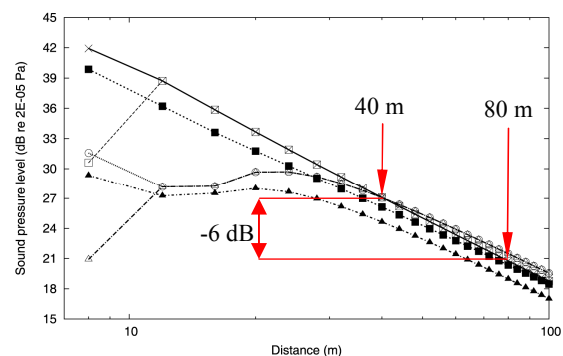


Figure 25 Changes in the sound pressure with distance from the center of the joint at 300° to Load-3. —X— 110 Hz; —□— 122 Hz; —■— 149 Hz; —○— 282 Hz; —△— 332 Hz; —▲— 392 Hz.

The directivity pattern for the sound calculated with a harmonic load at 149 Hz (lower frequency with dominant sound pressure peak inside the cavity) is presented in Figure 24 for 12 m from the center of the expansion joint, as an example. Figure 25 shows the changes in the sound pressure with distance from the center of the expansion joint for some frequencies at which dominant sound pressure peaks inside the cavity were observed. The sound pressure was obtained at an angle of 300° that corresponds to the direction of one of the main lobes in the directivity patterns for all frequencies investigated. Figure 25 shows that the change in the sound pressure is not uniform at

distances closer than 35 m possibly because of the near field effect of the sound source. At distances farther than 35 m, the sound pressure decreases by approximately 6 dB with doubling the distance from the source, which is a sign of far field for the joint–cavity system.

Conclusions from this study that may be applicable to the noise generation and radiation from modular expansion joints with different sizes and configurations are: 1) the noise from the bottom side of the joint was caused by the excitation of the structural modes of the expansion joint and/or acoustic modes of the cavity beneath the joint, which is consistent with an earlier conclusion derived from a full-scale model of a modular expansion joint; 2) the sound radiation efficiency of the joint–cavity system appeared to be high at natural frequencies of vibration modes of the joint with significant vertical vibration of center and support beams; 3) noise from the joint–cavity system may be propagated most effectively at radiation angles of acoustic modes of the cavity, which can be predicted roughly from the fundamental theory of sound radiation from cavities and waveguides; 4) the boundary between near field and far field in the sound field around the joint–cavity system may be predicted approximately by the previous findings of the characteristics of radiation field of a sound source by considering the greater dimension of the cavity cross-section as the maximum source dimension.

8. HUMAN RESPONSE TO VIBRATION

The research activities within the group include studies of the effects of vibration on people. The results obtained from those studies could improve understanding of human responses to vibration and be applied to, for example, the assessment of vibration environment, which is experienced in various transports, typically, and civil engineering structures such as bridges. The studies conducted within the period covered by this report include those of the subjective responses (i.e., feeling or sensation to vibration), the biodynamic responses (i.e., the mechanical response of the body to vibration), and the relation between the two responses.

8.1 Human vibration perception thresholds

Vibration has been recognized as one of the seven typical causes of the environmental problem in residential areas in Japan. For the recent several years, the number of complaints against vibration has been increasing, particularly in city areas. It is stated in ISO 2631-2 that “experience in many countries has shown that adverse comments regarding building vibration in residential situations may arise from occupants of buildings when the vibration magnitudes are only slightly in excess of per-

ception levels”. As indicated in this statement, understanding of the characteristics of human perception of vibration is important in vibration evaluation and assessment in the residential environment. An experimental investigation of human vibration perception thresholds has been conducted in the group (Matsumoto et al. 2011). The objective of this study was to investigate the effect of gender and age of subjects and vibration duration on human perception thresholds of vertical whole-body vibration experimentally.

Some factors that may affect human perception thresholds of the vertical whole-body vibrations were investigated in two laboratory experiments with recumbent subjects. A recumbent position was selected as the position of the subject because vibration problems in residential environments are often raised at night or early in the morning when people are asleep or about to sleep.

In the first experiment, the effects of gender and age of subjects on perception were investigated with three groups of 12 subjects, i.e., young males, young females and old males. For continuous sinusoidal vibrations at 2, 4, 8, 16, 31.5 and 63 Hz, there were no significant differences in the perception thresholds between male and female subjects, while the thresholds of young subjects tended to be significantly lower than the thresholds of old subjects (Figure 26).

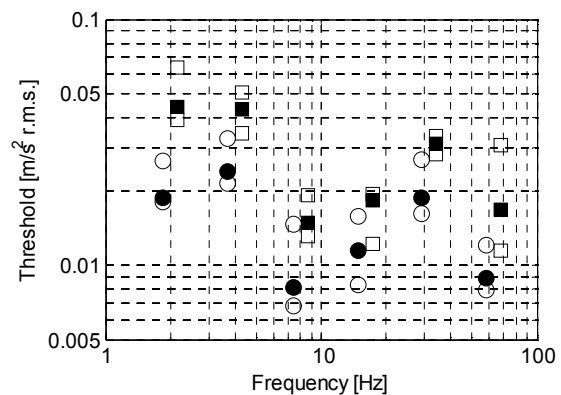


Figure 26 Medians and inter-quartiles of the perception thresholds of the continuous vibrations for male subjects in their twenties and in their sixties. ●: medians of subjects in their twenties, ○: 25 and 75 percentiles of subjects in their twenties, ■: medians of subjects in their sixties, □: 25 and 75 percentiles of subjects in their sixties.

In the second experiment, the effect of vibration duration was investigated by using sinusoidal vibrations, at the same frequencies as above, modulated by the Hanning windows with different lengths (i.e., 0.5, 1.0, 2.0 and 4.0 s) for 12 subjects. It was found that the peak acceleration at the

threshold tended to decrease with increasing duration of vibration. The perception thresholds were also evaluated by the running root-mean-square (r.m.s.) acceleration and the fourth power acceleration method defined in the current standards. The differences in the threshold of the transient vibrations for different durations were less with the fourth power acceleration method. Additionally, the effect of the integration time on the threshold was investigated for the running r.m.s. acceleration and the fourth power acceleration. It was found that the integration time that yielded less differences in the threshold of vibrations for different durations depended on the frequency of vibration.

8.2 Biodynamic response

8.2.1 Modelling resonances of the standing body exposed to vertical whole-body vibration

In the previous experimental study (Subashi et al. 2006), the vertical apparent mass and the fore-and-aft cross-axis apparent mass of the human body standing in five different postures (i.e., ‘upright’, ‘lordotic’, ‘anterior lean’, ‘knees bent’, and ‘knees more bent’) were determined. A study was conducted to investigate the dynamic motion of the body associated with resonances in the vertical apparent mass and the fore-and-aft cross-axis apparent mass of the standing body observed in the experiment (Subashi et al. 2008). It was desired to develop lumped parameter mathematical models that reflect some attributes of anatomical parts of the body so as to obtain an insight into the body motions associated with the resonances observed in different postures. Lumped parameter mathematical models representing anatomical parts of the human body have been developed (Figure 27). The inertial and geometric parameters of the models were determined from published anthropometric data. Stiffness and damping parameters were obtained by comparing model responses with experimental data obtained previously.

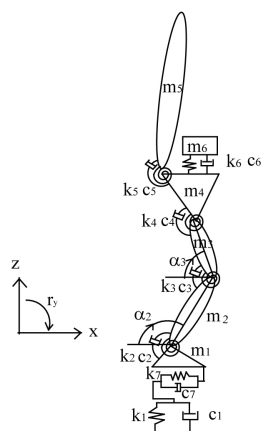


Figure 27 Schematic diagram of a multi-degree-of-freedom lumped parameter models of human body in a standing position

The principal resonance of the vertical apparent mass, and the first peak in the fore-and-aft cross-axis apparent mass, of the standing body in an upright posture (at 5–6 Hz) corresponded to vertical motion of the viscera in phase with the vertical motion of the entire body due to deformation of the tissues at the soles of the feet, with pitch motion of the pelvis out of phase with pitch motion of the upper body above the pelvis. Upward motion of the body was in phase with the forward pitch motion of the pelvis. Changing the posture of the upper body had minor effects on the mode associated with the principal resonances of the apparent mass and cross-axis apparent mass, but the mode changed significantly with bending of the legs. In legs-bent postures, the principal resonance (at about 3 Hz) was attributed to bending of the legs coupled with pitch motion of the pelvis in phase with pitch motion of the upper body. In this mode, extension of the legs was in phase with the forward pitch motion of the upper body and the upward vertical motion of the viscera.

8.2.2 Horizontal apparent mass of the standing human body

The driving-point dynamic responses of standing people (e.g. their mechanical impedance or apparent mass) influence their dynamic interactions with structures on which they are supported. The apparent mass of the standing body has been reported previously for vertical excitation but not for lateral or fore-and-aft excitation. The objective of this study was to advance understanding of the characteristics of the driving-point dynamic responses of standing people exposed to horizontal vibration. An experiment was conducted to measure the dynamic responses of standing subjects exposed separately to fore-and-aft and lateral vibration of the surface on which they were supported. Twelve standing male subjects were exposed to fore-and-aft and lateral random vibration over the frequency range 0.1 to 5.0 Hz for 180 s at four vibration magnitudes: 0.016, 0.0315, 0.063, and 0.125 ms⁻² r.m.s. With lateral excitation at 0.063 ms⁻² r.m.s., subjects also stood with three separations of the feet.

The dynamic forces measured at the driving-point in each of the three translational axes (i.e. fore-and-aft, lateral and vertical) showed components not linearly related to the input vibration, and not seen in previous studies with standing subjects exposed to vertical vibration or seated subjects exposed to vertical or horizontal vibration. A principal peak in the lateral apparent mass around 0.5 Hz tended to decrease in both frequency and magnitude with increasing magnitude of vibration and increase with increasing separation of the feet (Figure 28). The fore-and-aft apparent mass appeared to peak at a frequency lower than the lowest frequency used in the study.

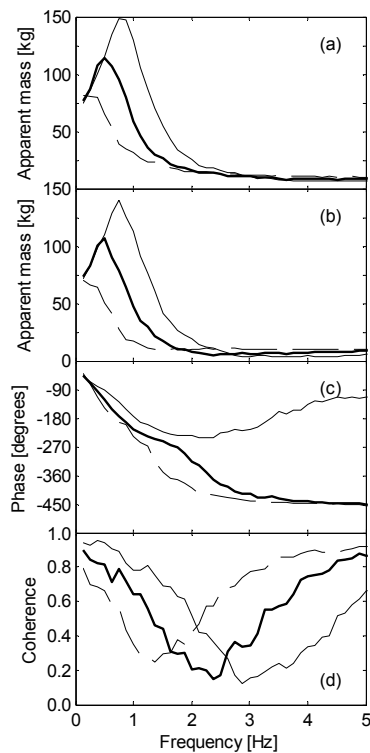


Figure 28 Median lateral apparent mass, phase and coherence for twelve subjects with three different separations of the feet at 0.063 ms^{-2} r.m.s.: (a) apparent masses calculated by the PSD method, (b) apparent masses calculated by the CSD method, (c) phases, (d) coherencies. Dashes: 0.15 m; solid, bold: 0.3 m; solid: 0.45 m.

8.3 Relation between dynamic and subjective responses

The effect of the magnitude of fore-and-aft and lateral vibration on the subjective and mechanical responses of seated subjects has been investigated experimentally using simultaneous measurements of relative discomfort and apparent mass (Subashi et al. 2008). Twelve male subjects were exposed to sinusoidal vibration at nine frequencies (between 1.6 and 10 Hz) at four magnitudes (in the range 0.125 to 1.0 ms^{-2} r.m.s.) in both horizontal directions (fore-and-aft and lateral). The method of magnitude estimation was used to estimate discomfort relative to that caused by a 4-Hz reference vibration in the same axis. The apparent mass was calculated from the acceleration and the applied force so as to quantify the mechanical response of the body. With each direction of excitation, the apparent mass was normalised by dividing it by the apparent mass obtained at 4 Hz, so that the mechanical responses could be compared with the subjective responses.

The relative discomfort and the normalised apparent mass were similarly affected by the fre-

quency and magnitude of vibration, with significant correlations between the relative discomfort and the normalised apparent mass (Figure 29). The results indicate that the discomfort caused by horizontal whole-body vibration is associated with the apparent mass in a frequency range where motion of the whole body is dominant. In this frequency range, the non-linear subjective responses may be attributed, at least in part, to the non-linear dynamic responses to horizontal whole-body vibration.

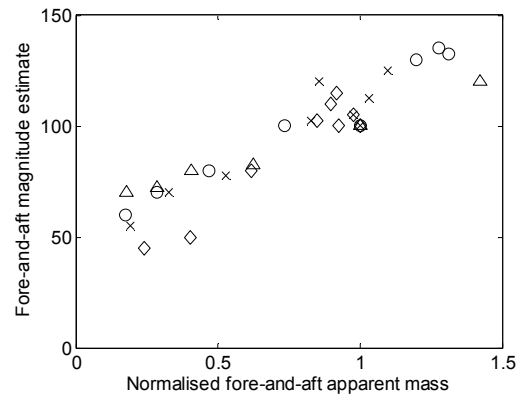


Figure 29 Median magnitude estimates compared with the normalised apparent mass for fore-and-aft vibration at four magnitudes: \diamond 0.125 ms^{-2} r.m.s., \times 0.25 ms^{-2} r.m.s., \circ 0.5 ms^{-2} r.m.s., Δ 1.0 ms^{-2} r.m.s.

9. REFERENCES

- Bhuiyan, A.R., Okui, Y., Mitamura, H., Imai, T. (2009) "A rheology model of high damping rubber bearings for seismic analysis: Identification of nonlinear viscosity", *International Journal of Solids and Structures* 46(7/8), pp.1778-1792.
- Imai, T., Bhuiyan, A.R., Razzaq, M.K., Okui, Y., Mitamura, H. (2010) "Experimental study of rate-dependent mechanical behavior of laminated rubber bearings", *Proc. of 7th Int. Conf. on Urban Earthquake Eng. & 5th Int. Conf. on Earthquake Eng.*, pp.1921-1928.
- Gull, J. H., Yamaguchi, H., Kumagai, K., Hung, P.V., Isozaki, M. (2011) "Interpretation of field-measured vibrations in transmission lines by gust response analysis", *Proceedings of the 9th International Symposium on Cable Dynamics*, 18-20 October, 2011, Shanghai, China.
- Ghimire, J. P., Matsumoto Y., Yamaguchi H. (2008) "Vibro-acoustic analysis of noise generation from a full scale model of modular bridge expansion joint", *Noise Control Engineering Journal*, 56 (6), pp.442-450.

Ghimire J. P., Matsumoto Y., Yamaguchi H., Kurahashi I. (2009) "Numerical investigation of noise generation and radiation from an existing modular expansion joint between prestressed concrete bridges", *Journal of Sound and Vibration*, 328, pp.129-147.

Gupta, V.K., Okui, Y., Nagai, M. (2006) "Development of web slenderness limits for composite I-girders accounting for initial bending moment", *Doboku Gakkai Ronbunshu A (J. of Structural Mechanics & Earthquake Engineering)*, JSCE, A 62(4) pp.854-864

Japan Road Association (2002) "Specifications for highway bridges", Part II: Steel bridge, Part V: Seismic design, Maruzen, Japan.

Juang, J. N. and Pappa, R. S. (1985) "An eigensystem realization algorithm for modal parameter identification and modal reduction", *Journal of Guidance, Control, and Dynamics* 8(5), pp.620-627.

Matsumoto Y., Griffin M.J. (2011) "The horizontal apparent mass of the standing human body", *Journal of Sound and Vibration*, 330, pp.3284-3297.

Matsumoto Y., Maeda S., Iwane Y., Iwata Y. (2011) "Factors affecting perception thresholds of vertical whole-body vibration in recumbent subjects: gender and age of subjects, and vibration duration", *Journal of Sound and Vibration*, 330, pp.1810-1828.

Matsumoto Y., Yamaguchi H., Tomida N., Kato T., Uno S., Hiromoto Y. and Khakimov A. (2007) "Experimental investigation of noise generated by modular expansion joint and its control". *Doboku Gakkai Ronbunshu A (J. of Structural Mechanics & Earthquake Engineering)*, JSCE, Vol. 63, No. 1, pp. 75-92 (in Japanese).

Matsumoto, Y., Yamaguchi, H., Yoshioka, T. (2010) "A field investigation of vibration-based structural health monitoring in a steel truss bridge", *IABSE-JSCE Joint Conference on Advances in Bridge Engineering-II*, August 8-10, 2010, Dhaka, Bangladesh, pp.461-467.

Ravshanovich, K. A., Yamaguchi, H., Matsumoto, Y., Tomida, N., Uno, Y. (2007) "Mechanism of noise generation from a modular expansion joint under vehicle passage", *Engineering Structures*, 29 (9), 2206-2218.

Subashi, G. H. M. J., Matsumoto, Y., Griffin, M. J. (2006) "Apparent mass and cross-axis apparent mass of standing subjects during exposure to vertical whole-body vibration", *Journal of Sound and Vibration*, 293, pp.78-95.

Subashi, G. H. M. J., Matsumoto Y., Griffin M. J. (2008) "Modelling resonances of the standing body exposed to vertical whole-body vibration: effects of posture", *Journal of Sound and Vibration*, 317, pp.400-418.

Subashi G. H. M. J., Nawayseh N., Matsumoto Y., Griffin M. J. (2009) "Non-linear subjective and dynamic responses of seated subjects exposed to horizontal whole-body vibration", *Journal of Sound and Vibration*, 321, pp.416-434.

Takeda, T., Sozen, M.A., Nielsen, N.N. (1970) "Reinforced concrete response to simulated earthquakes", *Journal of Structural Engineering*, 96:2557-2573.

Yamaguchi, H., Okui, Y., Matsumoto, Y. (2008) "Research activities of Structural Mechanics and Dynamics Group, Saitama University in 2004-2007", Research Report of Department of Civil and Environmental Engineering, Faculty of Engineering, Saitama University, 35, pp.1-14.

Yoshioka, T., Ito, S., Yamaguchi, H., Matsumoto, Y. (2010a) "Structural health monitoring of truss bridges based on damping change in diagonal member-coupled mode", *Doboku Gakkai Ronbunshu A*, 66 (3), pp.516-534. (In Japanese).

Yoshioka, T., Yamaguchi, H., Matsumoto, Y. (2010b) "Structural health monitoring of steel truss bridges based on modal damping changes in local and global modes", *Proceedings of the 5th World Conference on Structural Control and Monitoring*, 12-14 July, 2010, Tokyo, Japan, 5WCSCM-167.

Yoshioka, T., Takahashi, M., Yamaguchi, H., Matsumoto, Y. (2011) "Damage assessment of truss diagonal members based on frequency changes in local higher modes", *Proceedings of the 12th East Asia-Pacific Conference on Structural Engineering and Construction (EASEC-12)*, 26-28 January, 2011, Hong Kong, China (Procedia Engineering, 14, pp.3119-3126.